ACS APPLIED NANO MATERIALS

www.acsanm.org

Article

Sialyl-Tn Antigen-Imprinted Dual Fluorescent Core–Shell Nanoparticles for Ratiometric Sialyl-Tn Antigen Detection and Dual-Color Labeling of Cancer Cells

Shan Jiang,[⊥] Tianyan Wang,[⊥] Sandra Behren, Ulrika Westerlind, Kornelia Gawlitza,* Jenny L. Persson,* and Knut Rurack

Cite This: https://doi.org/10.1021/acsanm.2c03252

Read Online

ACCESS | Metrics & More | Article Recommendations | Supporting Information

ABSTRACT: Sialyl-Tn (STn or sialyl-Thomsen-nouveau) is a carbohydrate antigen expressed by more than 80% of human carcinomas. We here report a strategy for ratiometric STn detection and dual-color cancer cell labeling, particularly, by molecularly imprinted polymers (MIPs). Imprinting was based on spectroscopic studies of a urea-containing green-fluorescent monomer **1** and STn-Thr-Na (sodium salt of Neu5Acα2-6GalNAcα-*O*-Thr). A few-nanometer-thin green-fluorescent polymer shell, in which STn-Thr-Na was imprinted with **1**, other comonomers, and a cross-linker, was synthesized from the surface of red-emissive carbon nanodot (R-CND)-doped silica nanoparticles, resulting in dual fluorescent STn-MIPs. Dual-color labeling of cancer cells was achieved since both red and green emissions were detected in two separate channels of the microscope and an improved accuracy was obtained in comparison with single-signal MIPs. The flow cytometric cell analysis showed that the binding of STn-MIPs was significantly higher ($p < 0.001$) than that of non-imprinted polymer (NIP) control particles within the same cell line, allowing to distinguish populations. Based on the modularity of the luminescent core–fluorescent MIP shell architecture, the concept can be transferred in a straightforward manner to other target analytes.

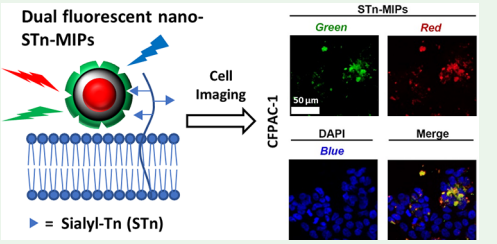

KEYWORDS: *cancer, core–shell particles, dual-color labeling, glycan, molecular imprinting*

INTRODUCTION

Glycosylation and other post-translational modifications, such as phosphorylation, acetylation, and amidation, are involved in the majority of biochemical processes at the cellular level in mammals and also in higher plants.[1] In protein *O*-glycosylation, (oligo)saccharides are conjugated to the hydroxyl groups of serine (Ser), threonine (Thr), or tyrosine (Tyr) residues. This group of modifications is important as structural or functional determinants for antibody recognition, mammalian cell adhesion, and microorganism binding.[2] The most common type of protein *O*-glycosylation, the mucin type, is initiated with *N*-acetyl-D-galactosamine (GalNAc) directly attached to the amino acid backbone. The GalNAc residue is often further extended into more complex and diverse glycan structures. However, in addition to the glycan structures found on healthy tissues, altered glycosylation involving sialylation, fucosylation, *O*-glycan truncation, and *N*- and *O*-linked glycan branching is often associated with cancer.[3] Thus, a certain type of tumor-associated glycans terminating with sialic acid (*N*-acetyl-neuraminic acid or Neu5Ac, abbrev. SA), Thomsen-nouveau or Tn (GalNAcα1-*O*-Ser/Thr), or sialyl-Thomsen-nouveau or STn (Neu5Acα2-6GalNAcα-*O*-Ser/Thr) antigen (Figure 1A) that result from altered glycosylation can serve as important biomarkers and provide a set of specific targets for diagnostic and therapeutic intervention.[4]

Recent achievements in the detection and identification of tumor-associated glycans and biomarkers would not have been possible without advancements in lectin discovery,[5] separation, and mass spectrometry techniques.[6] Additionally, molecular imprinting, a technique creating template-tailored cavities in polymer matrices through covalent or noncovalent bonds, has been adapted for the detection of glycans.[7−10] Particularly, fluorescent molecularly imprinted polymers (MIPs) appear as one of the most promising candidates in this regard due to the high sensitivity and ease of operation of fluorescence.[11−13] For instance, monosaccharide-imprinted fluorescent polymers have been developed as cell staining reagents with affinity and specificity to image cell surface molecules such as hyaluronan and SA-terminated glycans by fluorescence microscopy.[14−19]

However, conventional MIPs imprinted with monosaccharides can only show high affinity to polysaccharides owning their repeating unit with slight modifications.[20,21] Since tumor-associated glycans usually have non-repeating chemical

Received: July 25, 2022
Accepted: October 17, 2022

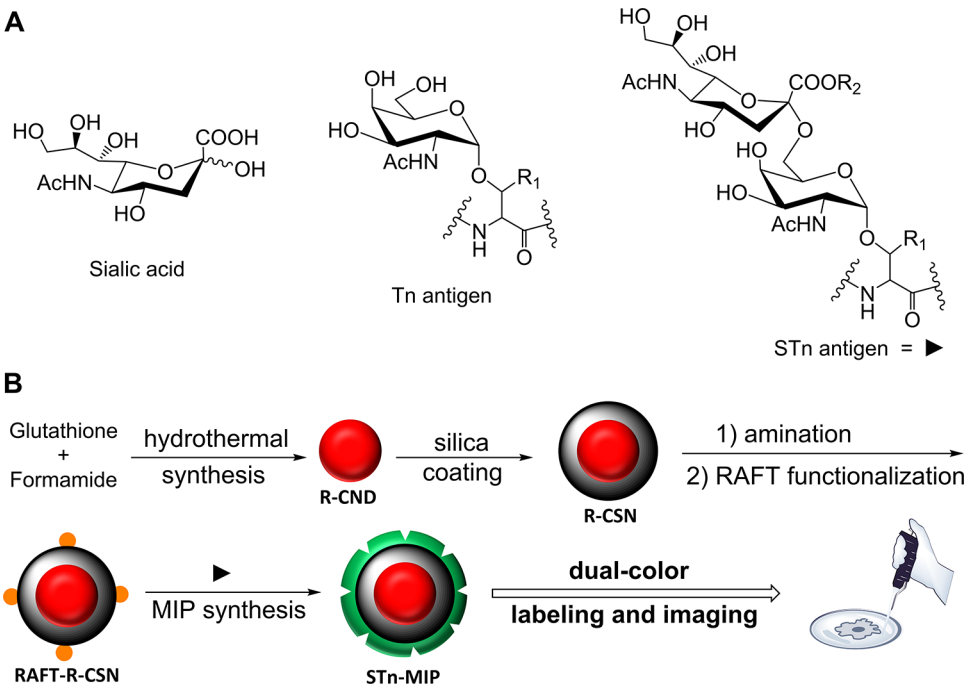

Figure 1. (A) Structure of tumor-associated monosaccharide (sialic acid, SA) and glycoconjugates (Tn antigen and STn antigen; R_1 = H, Tn/STn-Ser; R_1 = CH_3, Tn/STn-Thr; R_2 = OH, neutral STn-Thr/Ser; R_2 = O^-/Na^+, sodium salt of STn-Thr/Ser). (B) Schematic illustration of the synthesis of dual fluorescent STn-MIPs.

structures, the achievement of higher binding affinity and specificity to tumor cells in comparison to, for instance, MIPs against SA is suggested to largely rely on the use of more elaborate target structures such as, for instance, the STn antigen as a template because it only expresses on cancer cells. Sialylation on the other hand is a much more widespread biochemical modification, also being important for vital processes in embryonic development, neurodevelopment, immune responses, or somatic cell reprogramming.[22] Thus, for a better discrimination between normal and cancer cells, the imprinting of STn might be a promising strategy.

To the best of our knowledge, no STn antigen-imprinted polymer (nano)particles for cell staining applications have been reported. In addition, quantification of a target analyte using only the intensity changes of a single fluorescence emission signal in a certain wavelength range can sometimes be problematic because interferences can arise from a variety of analyte-independent factors, such as light scattering by the sample matrix, excitation source fluctuation, the microenvironment around a probe or variations of the local concentration of the probe.[23−26] Surprisingly, very little research has been reported on the preparation of dual fluorescent MIPs for glycan detection, although the correlation of two independent fluorescence signals from a shielded, inert particle core and an imprinted shell that can respond to target structures upon binding promises to yield more reliable data.

Here, we report on the development of green/red dual fluorescent nanoparticle probes that combine a red-emitting carbon nanodot core (R-CND) and a few-nanometer-thin green-fluorescent MIP layer, the latter being imprinted with the key disaccharide of tumor-associated glycans, the STn antigen, and their use in biomarker detection and cancer cell imaging (Figure 1B). Few-nanometer-thin MIP layers have been reported to guarantee fast equilibration times,[27,28] which is essential for instance for biomarker detection assays. The surface chemistry of MIP layers can be possibly tuned by further functionalization, for instance, PEGylation, which is an advantage of using nanoparticle stains in immunofluorescence staining, compared with fluorescent dyes. Both emissions of the nanoparticle probes were detected in fluorescence microscopy-based staining experiments of STn-positive CFPAC-1 cells, and an improved imaging accuracy was obtained, better matching with the flow cytometric cell analysis.

EXPERIMENTAL SECTION

Chemicals and Reagents. If not otherwise stated, solvents were purchased in the quality pro analysis (p.a.) and used without further purification. Dimethylformamide (DMF), dimethyl sulfoxide (DMSO), methanol, ethanol, tetrahydrofuran (THF), cyclohexane, toluene (anhydrous), acetone, acetonitrile (MeCN), hexane, petroleum ether (PE), Triton X-100, ethylchloroformate, formic acid, 4-cyano-4-(thiobenzoylthio)pentanoic acid (CPDB), (3-aminopropyl)-triethoxysilane (APTES), ethylene glycol dimethacrylate (EGDMA), 2-(dimethylamino)ethyl methacrylate (2D), D-(+)-glucose (Glc), D-(+)-galactose (Gal), and *N*-acetylglucosamine (GlcNAc) were purchased from Sigma-Aldrich, *n*-hexanol, 4-vinylphenylboronic acid (VBA), D-(+)-mannose (Man), and *N*-acetylgalactosamine (GalNAc) from Alfa Aesar, 2,2′-azobis(2,4-dimethyl)valeronitrile (ABDV) from Wako Chemicals, anhydrous DMF and anhydrous THF from Acros, chloroform (spectroscopic grade), acetonitrile (spectroscopic grade), tetraethylorthosilicate (TEOS), and sodium acetate (NaOAc) from Merck, ammonia (32%) from Applichem, and formamide and sialic acid (SA) from Roth. Fluorescent monomer **1** was synthesized by following the literature.[27] The synthesis of STn-Thr-Na can be found in the Supporting Information. Milli-Q water was drawn from a Milli-Q ultrapure water purification system (Millipore Synthesis A10).

Preparation and Characterization of Dual Fluorescent Core−Shell STn-MIP and NIP Nanoparticles. *Synthesis and Functionalization of Fluorescent Core Nanoparticles.* The synthesis of the red carbon nanodots (R-CNDs) was adapted from the literature.[29] Briefly, 20 mL of glutathione formamide (3 wt %) solution was transferred into a Teflon-lined autoclave and heated at

https://doi.org/10.1021/acsanm.2c03252
ACS Appl. Nano Mater. XXXX, XXX, XXX−XXX

Scheme 1. Previous[15] and Proposed Equilibria for the Interaction Between the Urea Motif of Fluorescent Monomer 1 and SA/STn in Organic Media (TBA: Tetrabutylammonium)

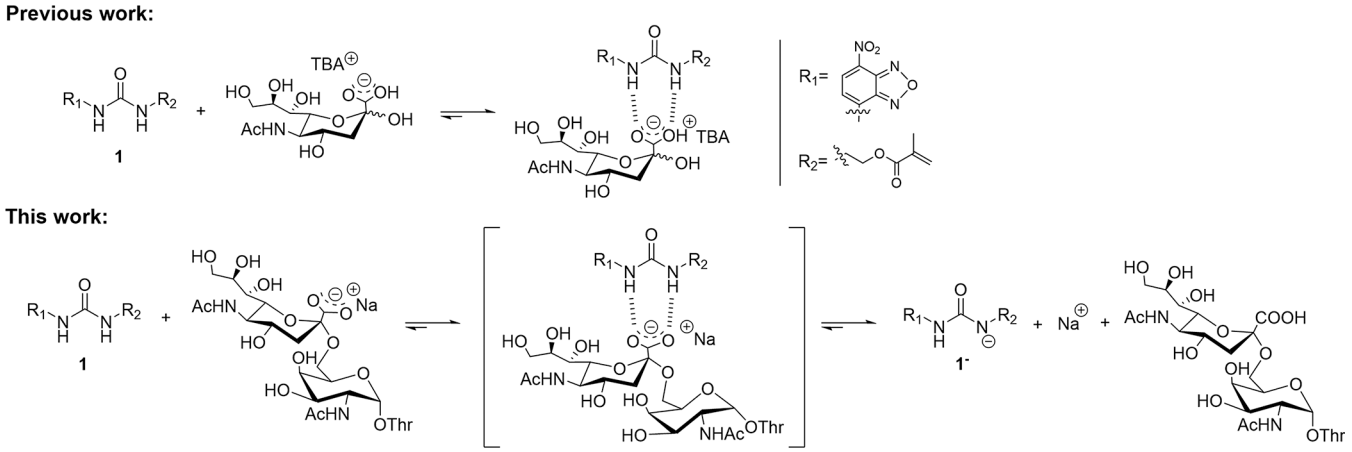

160 °C for 5 h. After the autoclave was left to cool to room temperature (RT), the reaction mixture was diluted 5-fold with Milli-Q water and precipitated by the addition of 100 mL of acetone. The precipitate was then washed with 20 mL of acetone once and methanol/acetone (10/90 vol %) three times (10 min centrifugation at 8900*g* for each washing step). Then, the residue was redispersed in methanol and filtered with a 0.22 μm membrane filter to remove large particle aggregates. After removal of methanol with a rotary evaporator, the sample was further dried at RT in a vacuum oven overnight.

The synthesis of the silica-coated red carbon nanodots (R-CSNs) followed a modified microemulsion method.[30] Typically, 17.7 g of Triton X-100, 77 mL of cyclohexane, 16 mL of *n*-hexanol and 3.4 mL of Milli-Q water were added into a 200 mL round-bottom flask and the resulting mixture was stirred for 15 min. An aqueous R-CND solution (0.4 mL, ca. 0.01 mg mL^{-1} in Milli-Q water at pH 2) was added to the emulsion and stirred for another 5 min, followed by the addition of 0.5 mL of TEOS. The hydrolysis of TEOS was initiated by adding 1 mL of 32% $NH_3 \cdot H_2O$, and the mixture was stirred at RT for 16 h, followed by the addition of ethanol to break the microemulsion and to recover the particles. The particles were washed twice with ethanol and once with water (50 mL, 10 min centrifugation at 8900*g* for each washing step) and dried at RT in a vacuum oven overnight.

Activation of the core particles with APTES and RAFT (reversible addition−fragmentation chain transfer) reagent (CPDB) functionalization for subsequent controlled RAFT polymerization was carried out as follows: to a solution of 1.0 g of R-CSNs in 120 mL of anhydrous toluene, 8 mL of APTES was added. The mixture was degassed for 30 min while heating up to 120 °C under reflux. The reaction was kept stirring for 24 h under argon (Ar) atmosphere. Afterward, APTES-R-CSNs were precipitated by adding 20 mL of cyclohexane, washed three times with 150 mL of toluene (5 min centrifugation at 8900*g* for each washing step), and dried in a vacuum oven overnight. To a solution of 190 mg of CPDB in 20 mL of anhydrous THF, 65 μL of ethylchloroformate and 94 μL of triethylamine were added and the mixture was flushed with Ar while stirring. The mixture was kept at −78 °C for 40 min under Ar atmosphere. In the meantime, 0.8 g of APTES-R-CSNs were dissolved in 10 mL of anhydrous THF, flushed with Ar, and kept at −10 °C. Cooled APTES-R-CSNs were added to the CPDB mixture under an Ar atmosphere (using a syringe) and stirring was continued for 24 h at RT. The nanoparticles (RAFT-R-CSNs) were precipitated with 40 mL of PE and washed three times with 100 mL of THF (5 min centrifugation at 8900*g* for each washing step) before drying at RT in a vacuum oven overnight.

Synthesis of STn-MIP and NIP Shells on CSN Cores. STn-Thr-Na was used as a template for the synthesis of STn-MIP particles. To the degassed (by Ar purging for 10 min) mixture of RAFT-R-CSNs (30 mg) in anhydrous DMF (3.5 mL), template, e.g., STn-Thr-Na (2.64 mg), VBA (0.64 mg), **1** (1.44 mg), 2D (5.8 μL), EGDMA (10.5 μL), and ABDV (3.5 mg) were added and the mixture was degassed for another 30 min in an ice bath (ca. 4 °C). The mixture was further stirred for 18 h at 50 °C and then for 2 h at 70 °C for polymerization. After adding 10 mL of hexane, the synthesized particles were washed once with DMF and three times with methanol (10 min centrifugation at 8900*g* for each washing step). For removal of the template, a mixture of 80% methanol, 15% formic acid, and 5% water was used to wash both STn-MIPs and NIPs for 1 h on a rotator at 40 rotations/min. After washing three times with a methanol/formic acid/water mixture (80/15/5 vol %), STn-MIPs and NIPs were washed once with methanol (10 min centrifugation at 8900*g* for each washing step) and further dried in a vacuum oven at RT overnight. The NIP particles were synthesized as control particles under the same conditions without using the template.

Particle Characterization. The diameter of the nanoparticles was determined from transmission electron microscope (TEM) measurements. The 0.5 mg mL^{-1} particle suspensions were prepared in absolute ethanol and 9 μL placed on a copper grid with a carbon film for TEM measurements. Images were analyzed with ImageJ software (National Institutes of Health and the Laboratory for Optical and Computational Instrumentation).[31] To determine the diameter of the particles, data from 100 particles were collected, and the average and standard deviation of the measurements were calculated. The chemical composition of nanoparticles was analyzed by thermogravimetric analysis (TGA) and elemental analysis (EA). Experimental details can be found in the Supporting Information.

Spectroscopic Studies. For the measurement of the interaction of **1** with STn-Thr-Na and the pre-polymerization mixture, microcells with a path length of 100 μm were used. For the titration of STn-MIPs and NIPs, cells with a path length of 1 cm were used and equipped with a magnetic stirring bar. Fluorescence spectra were measured with a FluoroMax 4 spectrofluorometer (HORIBA Scientific). Absorption spectra and spectrophotometric titrations were acquired with a Specord 210 Plus spectrometer (Analytik Jena). Experimental details can be found in the Supporting Information.

Immunofluorescence (IF) Staining and Flow Cytometry (Fluorescence-Activated Cell Sorting, FACS) Assays. BxPC-3 (RRID: CVCL_0186) and CFPAC-1 (RRID: CVCL_1119) cell lines were purchased from American Type Culture Collection (ATCC, Manassas, VA). For IF staining, cells were seeded on glass coverslips for overnight culture, followed by fixation with 4% paraformaldehyde, and stained with antibodies, STn-MIPs and NIPs. For FACS assays, cells were stained with antibodies, STn-MIPs and NIPs without fixation. Cell culture conditions and other experimental details can be found in the Supporting Information.

https://doi.org/10.1021/acsanm.2c03252
ACS Appl. Nano Mater. XXXX, XXX, XXX−XXX

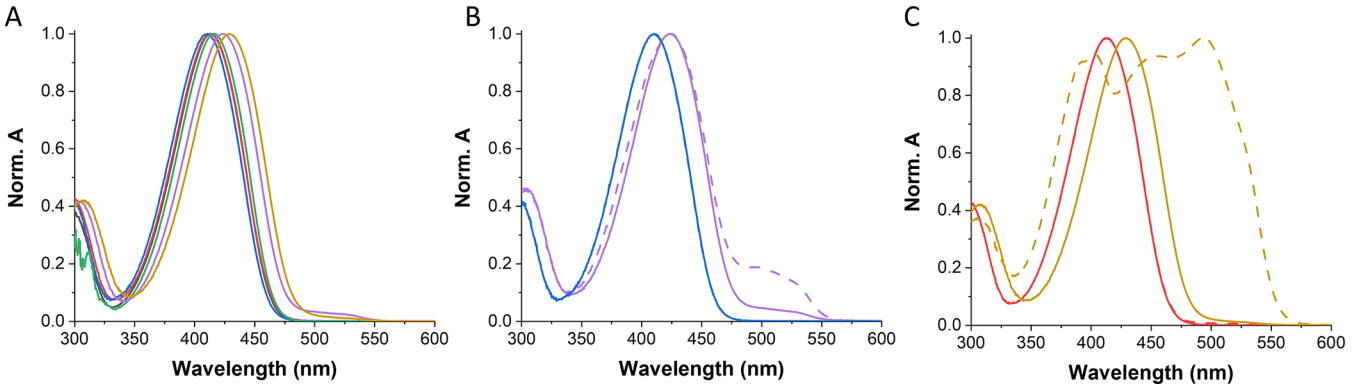

Figure 2. Normalized absorption spectra of **1** (1 mmol L^{-1}) in (A) different organic solvents (acetone, black; MeCN, red; $CHCl_3$, blue; cyclohexanone, green; DMF, purple; DMSO, ochre), (B) $CHCl_3$ (blue) and DMF (purple) in the absence (solid) and presence (dashed) of 1 equiv of NaOAc, and (C) MeCN (red) and DMSO (ochre) in the absence (solid) and presence (dashed) of 1 equiv of NaOAc.

RESULTS AND DISCUSSION

Although newly developed analyte-responsive MIPs have been reported in recent years, relatively little effort has been directed toward understanding the underlying mechanism by which recognition of a template by a mixture of monomers and cross-linkers is transduced into a measurable signal, which is essential for the design and application of molecularly imprinted sensory polymers.[32,33] Thus, for signaling MIPs like the thin shells grafted from the red-emissive carbon nanodot-doped silica (R-CSN) core particles as in the present case, it is important to know that the recognition mechanism of the fluorescent probe monomer and template in the synthesis solvent (largely organic) is retained in the medium of use (aqueous). The used comonomers and cross-linkers should therefore have an assistant effect without interfering the spectroscopic response.

Spectroscopic Study of STn-Thr-Na with Fluorescent Monomer 1 in DMF. STn-Thr carries two functionalities (Figure 1A), a carboxylic acid and a *cis*-diol unit, that can be addressed by supramolecular binding motifs (i.e., complementary groups in a recognition element, whether probe molecule or polymer, that can interact with these specific functional entities on an analyte/template) in a covalent or noncovalent fashion. These desired interactions play a decisive role in choosing the components, particularly, the fluorescent monomer, comonomer, and cross-linker, for the STn-MIP synthesis. It is well known that the *cis*-diol can be covalently reacted with a boronic acid-containing comonomer to form a five- or six-membered ring.[9,34] Previous studies also showed that the carboxylic acid moiety can be deprotonated by basic tetraalkylammonium (TXA) salts and further interacts with a urea-containing fluorescent monomer via two directional hydrogen bonds,[35,36] inducing spectroscopic changes that are desired for the use of MIP-based nanoparticles as probes or stains. For instance, the nitrobenzoxadiazole (NBD) chromophore modified with a urea motif (**1**, Scheme 1) served as the fluorescent monomer in the recognition of the tetrabutylammonium (TBA) salt of *Z*-L-phenylalanine through MIPs.[27]

However, when aiming beyond model studies in nonprotic organic solvents, i.e., aiming at cell culturing and *in vivo* studies in aqueous media, it has to be considered that the carboxylic acid moiety of a sugar acid like SA is most likely deprotonated (pK_a = 2.6 in the case of SA) and electrostatically associated with inorganic cations (e.g., Na^+, K^+, Ca^{2+}).[37] Imprinting highly hydrophilic carboxylates as TXA salts as it is commonly done for the imprinting of more lipophilic, small-molecule organic acids into MIPs prepared in organic solvents[38] would thus have an important disadvantage, i.e., the cavities formed would be essentially too large because the native inorganic cations present in the rebinding scenario are much smaller in size than TXA. Recently, we have shown that the type as well as electronic and chemical nature of a counterion used for imprinting becomes decisive for the resulting MIP performance already at the TXA level.[39] Furthermore, an exchange of the inorganic counterions of cell surface glycans for their TXA analogues *in situ* in the analytical assay is also not possible in cell-targeting applications, rendering the use of phase-transfer strategies impossible.[28] Additionally, using native salts such as STn-Thr-Na for imprinting is largely hampered by solubility reasons and, even if a salt might be soluble in a highly polar organic solvent, would be aggravated because ion pairing effects would be significant and interfere with the desired interaction of the carboxylate with the fluorescent monomer's binding site to generate the analytical signal. Searching for an alternative approach thus became important.

To get a better understanding of the interaction of fluorescent monomer **1** with sodium salts of an aliphatic carboxylate such as STn in organic solvents potentially suitable for polymerization, sodium acetate (NaOAc) was used as a model analyte. The experiments were thus carried out at pre-polymerization conditions, i.e., at concentrations that are identical with the concentrations used in MIP synthesis. To determine the most suitable porogen for the formation of tight binding cavities during the MIP synthesis, solvents with different polarities and H-bonding strengths have been investigated. Because the solvent is always present in a high excess in its role as porogen, only hydrogen bond-accepting solvents that do not block the carboxylate group of the template and show a much weaker binding tendency to the urea group of **1** than a carboxylate group were used. Figure 2A shows that the longest wavelength absorption band of **1** (centered at ca. 400 nm in $CHCl_3$) shifts in different organic solvents. An analysis of these absorption maxima with a range of established theoretical and empirical solvent polarity scales further suggested that the solvent-dependent shift correlates best with the polarity and the H-bond acceptor strength of the different solvents and is thus, most likely, an effect of both solvent properties (Table S1). In DMSO and DMF, the solvents with the highest polarity and H-bond acceptor strength, the red shift of the main absorption band of **1** is most pronounced (ca. 10 nm). This is most likely resulting

https://doi.org/10.1021/acsanm.2c03252
ACS Appl. Nano Mater. XXXX, XXX, XXX−XXX

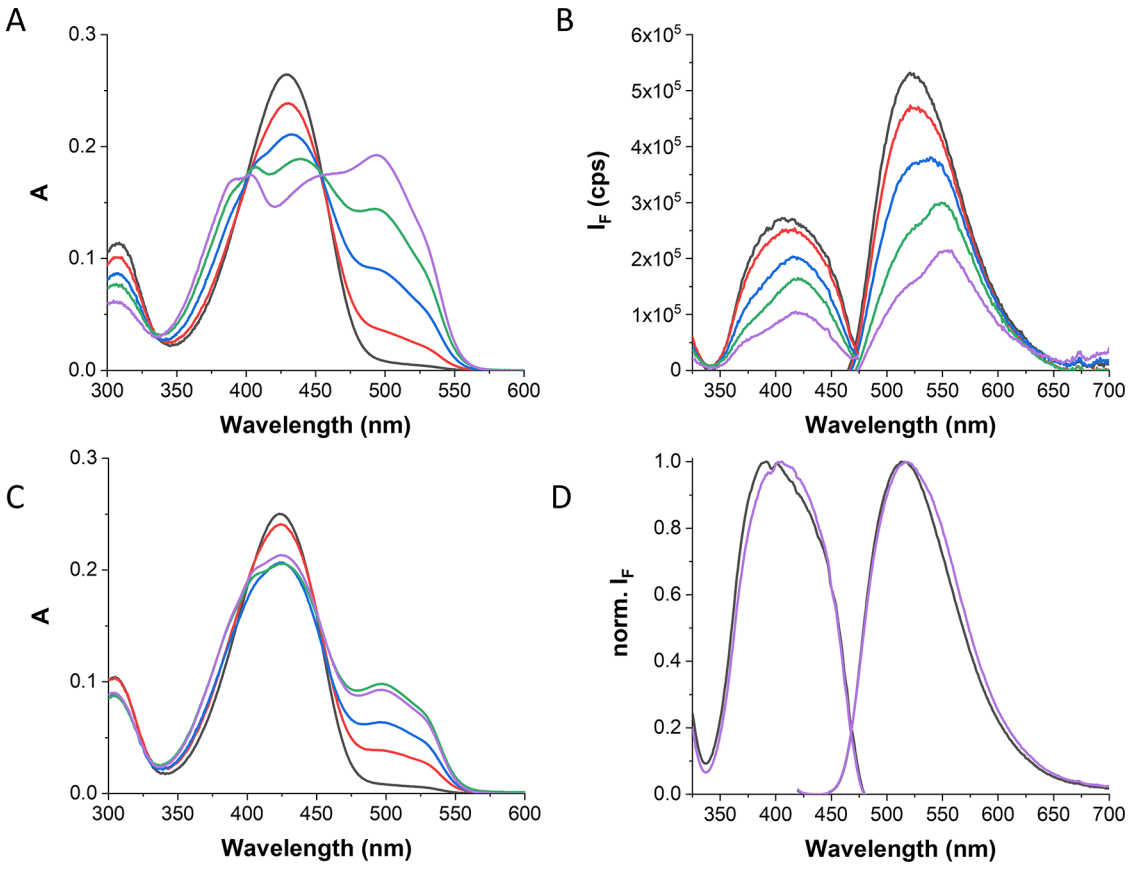

Figure 3. (A) Absorption and (B) fluorescence excitation (λ_{em} 490 nm) and emission (λ_{ex} 410 nm) spectra of **1** (1 mmol L^{-1}) with 0−0.7 equiv of NaOAc in DMSO. (C) Absorption and (D) normalized fluorescence excitation (λ_{em} 490 nm) and emission (λ_{ex} 410 nm) spectra of **1** (1 mmol L^{-1}) with 0−0.7 equiv of NaOAc in DMF; 0 equiv NaOAc (black), 0.1 equiv NaOAc (red), 0.3 equiv NaOAc (blue), 0.5 equiv NaOAc (green), and 0.7 equiv NaOAc (purple).

from the hydrogen bond-accepting character of the oxygen atoms in both solvents, forming an N−H···O bond with **1**.[40] However, compared with the 30 nm bathochromic shift generally induced through complexation of a carboxylate at equimolar concentrations,[27] the interaction between the solvents and the fluorescent monomer are supposedly distinctly weaker. Additionally, in DMSO and DMF, the slight onset of a second absorption band at ca. 500 nm can be observed (Figure 2A), which is known to indicate the presence of the anionic form of **1** (**1**$^-$, Scheme 1).[27,41]

When adding 1 equiv of our model analyte NaOAc, spectroscopic effects in $CHCl_3$ and MeCN are absent because too strong ion pairing of Na^+ and AcO^- induces low solubility in these solvents and precludes H-bonding between **1** and AcO^-. In contrast, strong spectroscopic effects are observed in DMSO and DMF (Figure 2B,C). Since a possible optical detection of the template after MIP synthesis relies on successful imprinting of the template in close vicinity to the dye molecule, strong spectroscopic effects at pre-polymerization conditions are necessary. Thus, the interactions taking place in DMSO and DMF have been investigated in more detail.

Fluorescent monomer **1** was titrated with NaOAc in DMSO and DMF under pre-polymerization conditions (Figure 3). Upon the addition of up to 0.7 equiv of NaOAc in DMSO, the main absorption band of **1** at ca. 410 nm decreases, while the band of **1**$^-$ at ca. 500 nm increases (Figure 3A). When exciting in the main absorption band at 410 nm, a strong decrease in the emission band at ca. 530 nm accompanied by the appearance of a second red-shifted emission band at >550 nm is observed (Figure 3B). This weaker fluorescence band presumably stems from **1**$^-$, which is supported by obtaining an emission band at ca. 575 nm when directly exciting in the corresponding absorption band (500 nm, Figure S1B). Additionally, the excitation spectra of this band nicely demonstrate the appearance of **1**$^-$ upon addition of the template in DMSO (Figure S1A).

To investigate the possible formation of hydrogen bonds between **1** and NaOAc in DMSO, an NMR titration was carried out. As shown in Figure 4, the two urea protons were slightly shifted to lower field upon the addition of NaOAc, which indicates that hydrogen bonds might be formed between urea hydrogens and acetate. Upon the addition of 0.9 equiv NaOAc, the deprotonation of **1** started to occur since one proton peak was almost absent. This was validated by the addition of 1 equiv of tetraethylammonium-hydroxide (TEA-OH), inducing the formation of **1**$^-$ due to its highly basic character.

Upon the addition of up to 0.7 equiv of NaOAc in DMF, the absorption band at ca. 500 nm increases as well, yet to a lesser extent than in DMSO (Figure 3C). When exciting in the main absorption band at 410 nm, only a slight decrease of the emission band at ca. 530 nm is observed with no appearance of a second red-shifted emission band, which would be expected if **1**$^-$ would have been formed (Figure 3D). Even after exciting at the absorption wavelength of the deprotonated species (500

https://doi.org/10.1021/acsanm.2c03252
ACS Appl. Nano Mater. XXXX, XXX, XXX−XXX

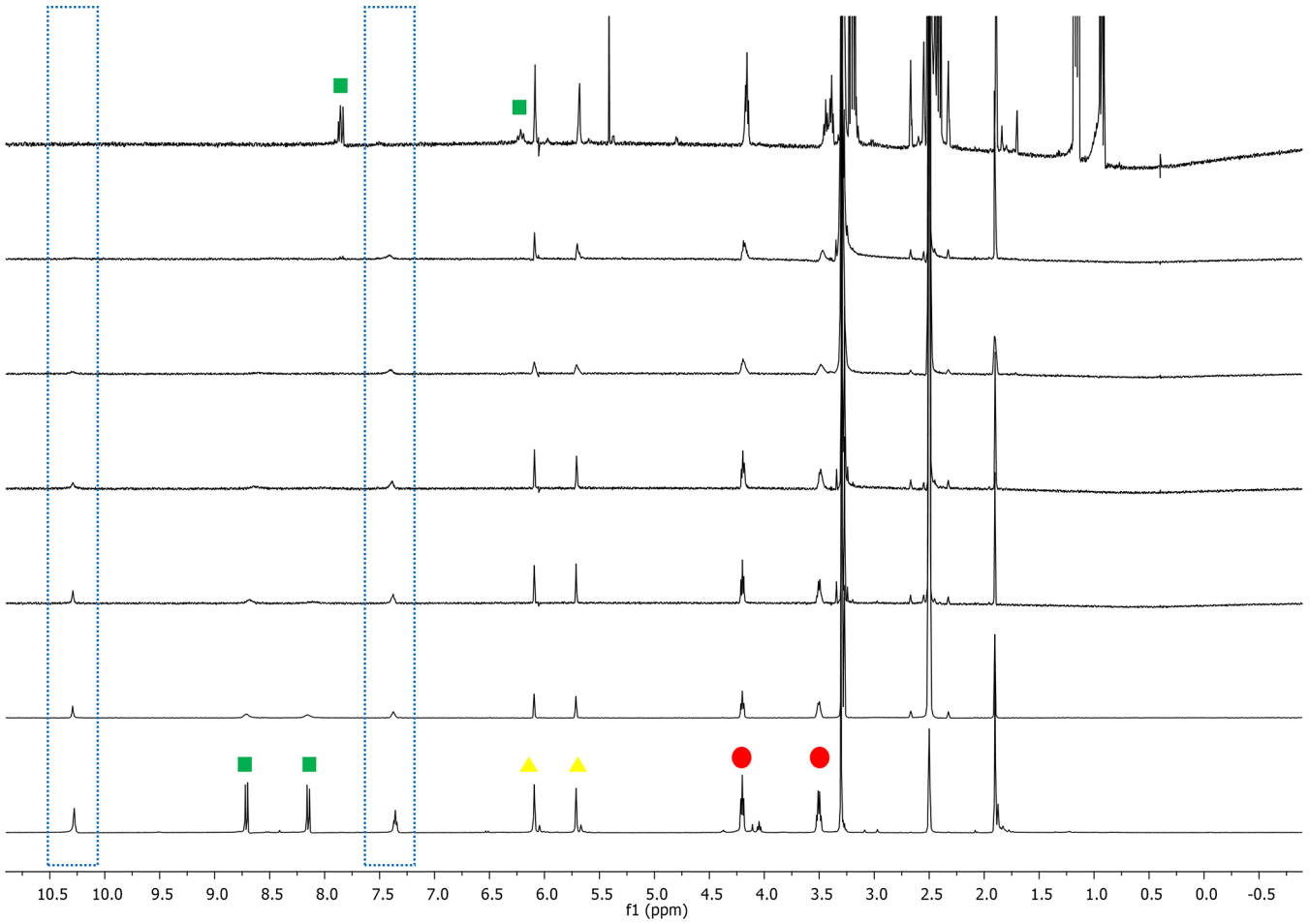

Figure 4. ^{1}H NMR spectra of **1** with 0–0.9 equiv NaOAc (bottom to top) and 1 equiv TEA-OH (highest) in DMSO-d_6. Urea protons are highlighted in the dotted blue area. Green square: aromatic protons; yellow triangle: CH_2 in methacrylate; red circle: 2 × CH_2 [**1** = 1 mmol L^{-1}].

nm), virtually no fluorescence emission was observed in the red region (Figure S1D). However, since the corresponding absorption band is stemming from the deprotonated species $\mathbf{1}^-$, which was confirmed by measuring an absorption spectrum of $\mathbf{1}^-$ after addition of the strong base tetramethylammonium hydroxide (TMA-OH; Figure S1E), the absence of emission from this species suggests that the excited form of $\mathbf{1}^-$, $[\mathbf{1}^-]^*$, is reprotonated within the lifetime of this transient state. With DMF being a hydrogen bond-accepting solvent, this reprotonation is tentatively ascribed to occur from an acetic acid molecule (AcOH) being in close vicinity to $[\mathbf{1}^-]^*$. As we have recently shown for another carboxylate-containing analyte and another urea-expressing fluorescent monomer, excited-state proton transfer processes can occur in such host–guest ensembles.[42] To determine the equilibrium constant (K_{eq}) for the interaction of **1** with STn-Thr-Na (cf. Scheme 1), **1** was titrated with STn-Thr-Na, yielding a $\log K_{eq}$ = 3.0 in DMF (Figure S2A). The correlation of K_{eq} with different calculated electronic parameters of different sodium salts shows a linear regression ($R^2 \approx 0.92$) between $\log K_{eq}$ and the sum of the charges of the carboxylate group, i.e., the charges on the carbon and the two oxygen atoms (Figures 3C and S2A–D and Table S2; more details can be found in the Supporting Information). These results indicate that the fluorescent monomer **1** and the template, e.g., STn-Thr-Na, are in close vicinity to each other in DMF. Thus, DMF has been used as a porogen for the synthesis of STn-MIP nanoparticles.

Since the MIP synthesis is carried out in the presence of various other components such as comonomers and cross-linkers and it is important to verify whether the spectroscopic behavior under MIP synthesis conditions is phenomenologically similar, pre-polymerization mixtures were investigated in more detail. To assist the formation of cavities in the MIP layer, 2-(dimethylamino)ethyl methacrylate (2D) and 4-vinylphenylboronic acid (VBA) were selected as comonomers. 2D was reported to act as a proton-accepting partner in aqueous media,[43,44] which can stabilize the deprotonated form of SA yet can also assist cyclic ester formation between boronic acid and the *cis*-diol moiety of SA by providing a basic environment (Figure 5B). Ethylene glycol dimethacrylate (EGDMA) has been chosen as the cross-linker because it is widely used in the synthesis of MIPs and helps to form a more hydrophilic polymer network for highly polar analytes and an application in polar media. In the presence of comonomers VBA and 2D, the cross-linker EGDMA, and the template STn-Thr-Na, the absorption spectrum was comparable with that from the spectroscopic studies discussed above (Figures 3C and S3). To obtain a polymer matrix with defined and tight imprinted cavities, a composition with a high cross-linking degree has been chosen. Thus, the MIP recipe was fixed to STn-Thr-Na/**1**/VBA/2D/EGDMA = 1:1:1:8:13 using DMF as the porogen. Because DMF has been previously used as a solvent for the synthesis of MIPs targeting SA, with satisfactory binding being obtained thereafter in water/organic solvent

https://doi.org/10.1021/acsanm.2c03252
ACS Appl. Nano Mater. XXXX, XXX, XXX–XXX

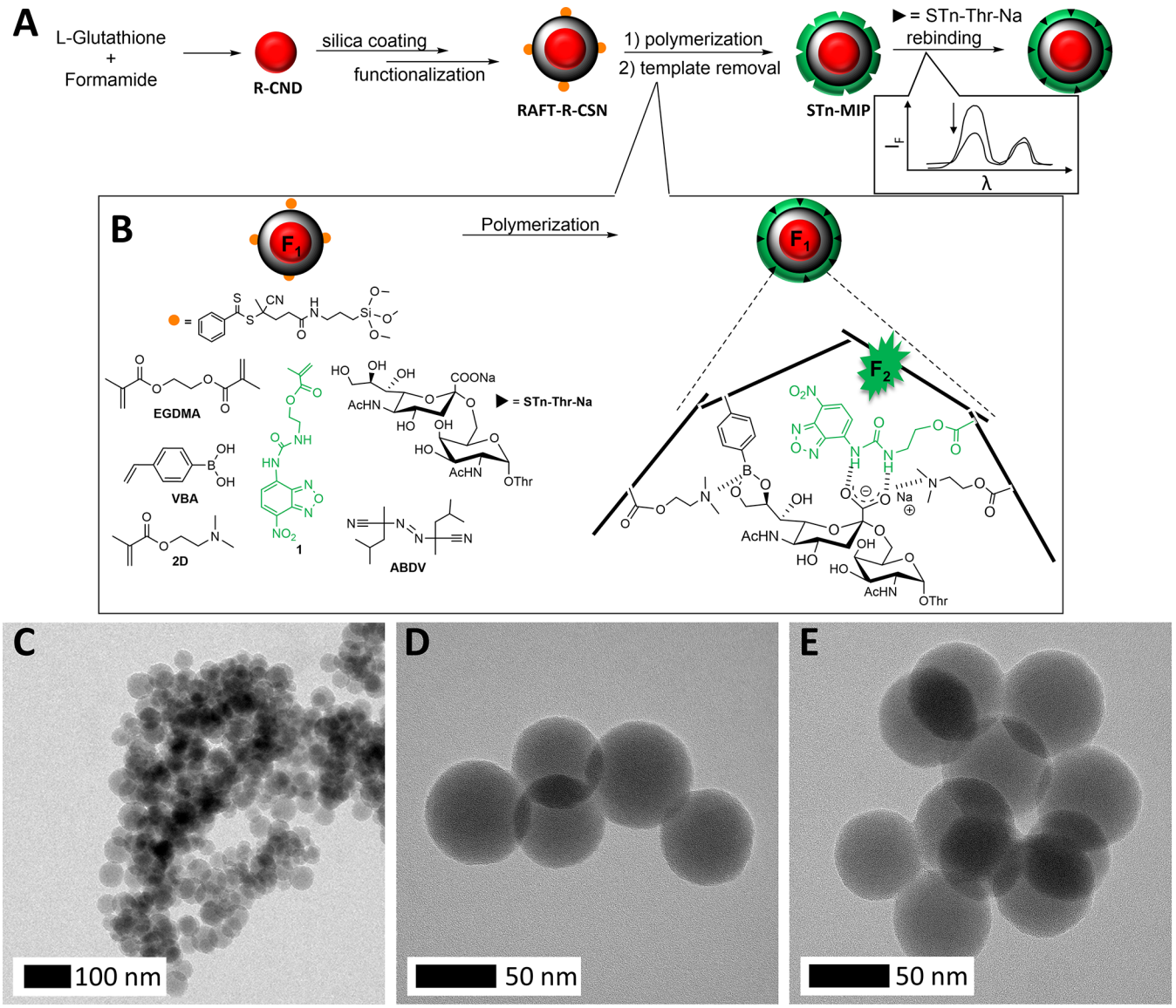

Figure 5. (A) Synthetic route toward dual fluorescent STn-MIP nanoprobes (ABDV: 2,2′-azobis(2,4-dimethyl)valeronitrile; for other abbreviations, see text). (B) Functional monomers and cross-linker used in STn-MIP synthesis and their interactions with the corresponding template in DMF. Representative TEM images of (C) R-CSNs, (D) STn-MIPs, and (E) NIPs.

mixtures[45] and aqueous buffers,[46,47] it was expected that fluorescent MIP particles synthesized in DMF could be used as well for STn labeling of cells in physiological buffers.

Preparation of Dual Fluorescent Core–Shell MIP Nanoparticles. Core–shell silica nanoparticle-based analytical approaches have been reported for a variety of applications in the fields of nanobiotechnology and life science. On one hand, the stability of a fluorescence signal can be enhanced by encapsulation of fluorophores into a silica matrix. On the other hand, the ability to synthesize particles with core–shell architectures allows multiple functions to be brought together in a single vehicle, separated in different compartments.[48] For instance, ratiometric fluorescent probes, following the core–shell architecture and having the potential to provide a rugged and reliable quantitative analysis in real time, are widely employed for chemo/biosensing and imaging of biomarkers.[49] Additionally, in comparison with traditional fluorescent dyes and conjugated antibodies, nanoparticles with a size ranging from 10 to 100 nm, such as modified carbon nanodots and quantum dots, possess alternative properties that enhance their imaging capabilities on fixed cells.[50] Accordingly, carbon nanodots (CNDs) have also recently been used in combination with conventional MIP shells for (bio)analytical applications.[51−53]

Thus, in addition to the green-fluorescent monomer **1**, which is polymerized in the STn-MIP layer, another fluorescence source ideally emitting at 650–950 nm[54] was embedded in the core. This second fluorescence can provide the reference signal for a ratiometric assay or it can improve the imaging of cancer cells *in vivo*. First, as shown in Figure 5A, red-emissive carbon nanodots (R-CNDs), which usually have excellent water solubility, resistance to photobleaching, and sub-10 nm size, were selected as the fluorescent reporters in the core material. R-CNDs, synthesized from glutathione, with an average size of 7.3 ± 1.1 nm determined by TEM, show a sharp emission band at 680 nm (excited at 410 nm) (Figure S4).

https://doi.org/10.1021/acsanm.2c03252
ACS Appl. Nano Mater. XXXX, XXX, XXX−XXX

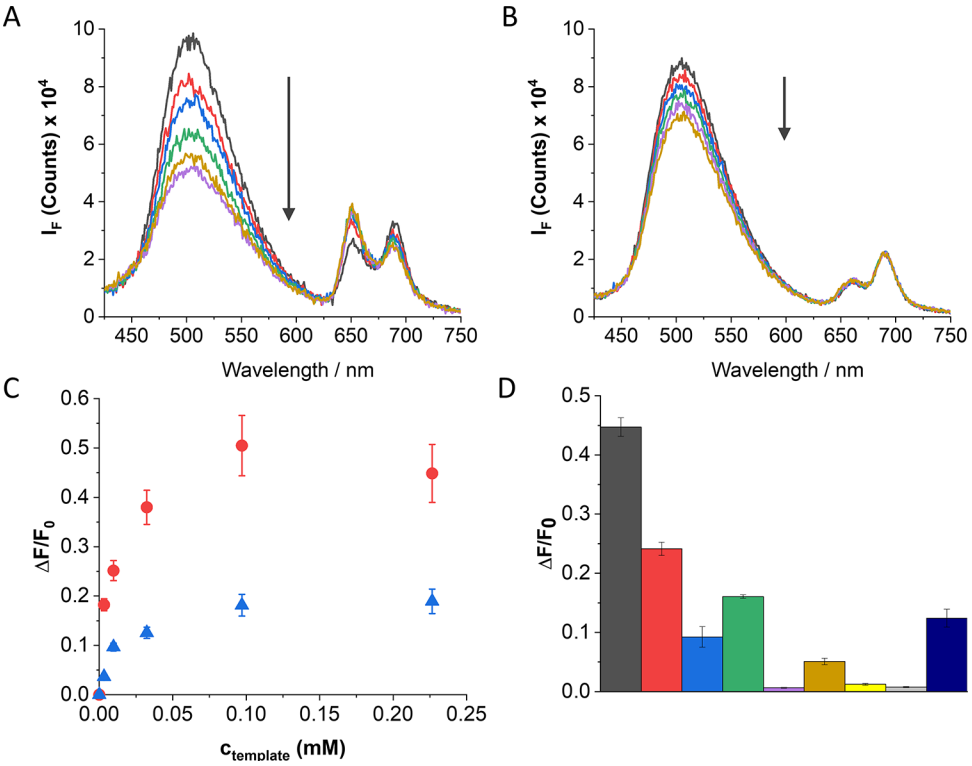

Figure 6. Representative fluorescence titration (λ_{ex} 410 nm) of (A) STn-MIPs and (B) NIPs upon the addition of 0−0.22 mmol L^{-1} STn-Thr in DMF. (C) Sensing response of STn-MIPs (red circles) and NIPs (blue triangles) toward STn-Thr-Na; [particles] = 0.5 g L^{-1}, DMF. (D) Sensing response of STn-MIPs toward STn-Thr-Na (black), NaOAc (blue), NaOBz (green), Glc (purple), Gal (ochre), Man (yellow), GlcNAc (grey), and GalNAc (navy) and of NIPs toward STn-Thr-Na (red); [particles] = 0.5 g L^{-1}, [STn-Thr-Na, competitors] = 0.22 mmol L^{-1}, DMF.

Second, aiming at a core−shell system with a STn-MIP layer as the shell, different functionalization steps have been performed. The silica-coating on R-CNDs was done by a water-in-oil (W/O) microemulsion approach, forming silica-coated red-emissive carbon nanodots (R-CSNs) with an average size of 46.1 ± 4.4 nm (Figure 5A,C). By comparing the material's properties of R-CSNs and plain silica particles (plain SiO_2) synthesized according to the same procedure, the incorporation of R-CNDs into the silica particles does not influence other material properties than the absorption and fluorescence (Figure S5).

Functionalization of the core particles with (3-aminopropyl)triethoxysilane (APTES) and 4-cyano-4-(thiobenzoylthio)pentanoic acid (CPDB), the reagent to grow the polymer network through reversible addition−fragmentation chain-transfer (RAFT) polymerization from the core particle's surface, led to particles with a RAFT agent density of ca. 0.1 mmol g^{-1}, which was determined by thermogravimetric analysis (TGA) and elemental analysis (EA) (Figure S6A,B). Finally, a STn-MIP shell using the template (STn-Thr-Na), **1**, VBA, 2D, and EGDMA in DMF with the ratios mentioned above was grafted from the surface, yielding monodisperse STn-MIPs with an average diameter of 65.1 ± 3.8 nm (Figure 5B,D). The nonimprinted analogues (NIPs) were synthesized as well using the same components except the template, yielding an average size of 64.4 ± 3.2 nm (Figure 5E).

Fluorescence Titrations of MIP and NIP Nanoparticles. To evaluate the (re)binding performance of STn-MIPs and NIPs in DMF, fluorescence titrations were conducted by adding STn-Thr-Na (up to 0.22 mmol L^{-1}) to suspensions of STn-MIP and NIP nanoparticles in DMF (0.5 g L^{-1}). As shown in Figure 6, both emission bands of **1** at 510 nm and R-CNDs at 680 nm are visible when excited at one wavelength (410 nm). The more structured emission band of R-CNDs in the STn-MIPs and NIPs compared to bare R-CNDs (Figure S4A) might be due to deprotonation and tautomerism when R-CNDs are embedded into the silica matrix.[29,55] The emission band at 680 nm remained largely unchanged in NIPs, while a slight change in the intensity ratio of the two subbands was found in the case of STn-MIPs upon addition of STn-Thr-Na. As the integral fluorescence remained constant within ±4.3%, this behavior does not influence the data measured with instruments such as microscopes or flow cytometers, which use filter sets in their detection channels. In contrast, a distinct fluorescence decrease was observed for the emission band of fluorescent monomer **1** (510 nm, Figure 6A), which could be explained by the deprotonation happening upon the addition of STn-Thr-Na that has been observed in the spectroscopic molecular interaction studies as well. However, as also observed in the studies with the model analyte NaOAc, no red-shifted emission band is observed, which again leads to the conclusion that the fraction of **1** that is deprotonated upon addition and diffusion of template/analyte into the polymer network is reprotonated by STn-Thr-Na, residing in close vicinity of the fluorescent probe, during the lifetime of $[\mathbf{1}^-]^*$. On the contrary, the addition of STn-Thr-Na to NIPs leads to a much weaker decrease of the emission band of the fluorescent monomer **1** (Figure 6B). Since the NIP particles are synthesized without the template being present, the polymer shell is simply a highly cross-linked network without any template-specific cavities but still with **1** being covalently integrated. Thus, STn-Thr-Na is most likely not able

https://doi.org/10.1021/acsanm.2c03252
ACS Appl. Nano Mater. XXXX, XXX, XXX−XXX

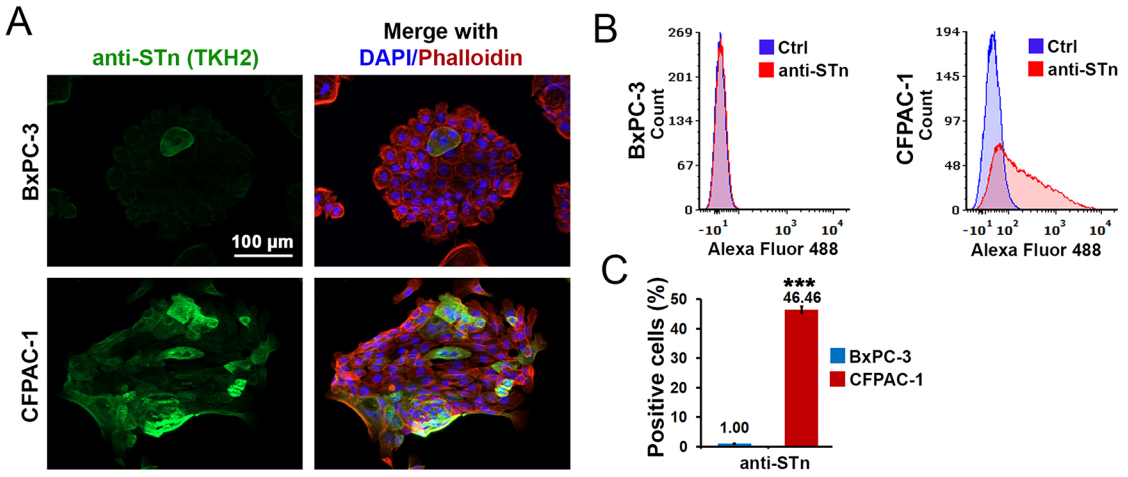

Figure 7. Analysis of STn expression on BxPC-3 and CFPAC-1 cell lines using (A) immunofluorescence staining (scale bar: 100 μm) and (B) flow cytometry after staining with STn-antibody TKH2; (C) percentage of STn-positive cells from the flow cytometry analysis.

to penetrate the network and thus not deprotonating **1** in the same extent as in the case of STn-MIPs.

For the performance assessment of STn-MIPs in solution, the fluorescence change $\Delta F/F_0 = (F_x - F_0)/F_0$, that is, the difference between the fluorescence intensity at analyte concentration x and the fluorescence intensity in the absence of the analyte at the maximum emission band at 510 nm divided by the initial fluorescence intensity, was determined and compared to the behavior of the corresponding non-imprinted beads. From the fluorescence changes at the saturation point, the so-called imprinting factor was determined as well (IF_{fl}) [eq 1]. In analogy to this, the discrimination against possible competitors is determined by the ratio of the fluorescence changes of the STn-MIPs titrated with STn-Thr-Na and the STn-MIPs titrated with a competitor yielding the discrimination factor DF_{fl} [eq 2].

$$IF_{fl} = \frac{(\Delta F/F_0)_{MIP}}{(\Delta F/F_0)_{NIP}} \quad (1)$$

$$DF_{fl} = \frac{(\Delta F/F_0)_{MIP,STn-Thr-Na}}{(\Delta F/F_0)_{MIP,competitor}} \quad (2)$$

As shown in Figure 6C, STn-MIPs exhibited a higher binding affinity to STn-Thr-Na in comparison to NIPs, yielding an IF_{fl} of 2.4. Additionally, the equilibrium constant ($\log K_{eq} = 3.1$) of STn-MIPs to STn-Thr-Na is in the same order of magnitude than that for **1** in DMF, hinting at the successful formation of cavities in the MIP shell and indicating a moderate binding affinity to the template in DMF. Different competitors have been tested as well to evaluate the selectivity of the STn-MIPs. Even if the sodium salt of SA would be the closest competitor to be tested because it is a subunit of STn-Thr-Na, it was not possible to obtain this salt. Thus, 0.22 mmol L^{-1} of NaOAc and NaOBz, which show similar K_{eq} as STn-Thr-Na (Table S2), were added to the nanoparticle suspension in DMF to investigate the discrimination against dimensionally smaller competitors that carry a carboxylic acid function, aliphatically and aromatically appended, representing a common motif in many samples of biological origin. Furthermore, five monosaccharides, glucose (Glc), galactose (Gal), mannose (Man), *N*-acetylglucosamine (GlcNAc), and GalNAc, were added as well, since they are common types of *O*-glycosylation in both normal and cancer cells.

Figure 6D shows that a weaker fluorescence decrease was found and thus weak binding of the competitors in comparison with the imprinted template, STn-Thr-Na, occurred, yielding DF_{fl} values of 4.9 and 2.8 for NaOAc and NaOBz, respectively. Due to the absence of a carboxylate moiety in the monosaccharides and thus less interaction with **1**, the DF_{fl} values were distinctly higher for those. This indicates that the synthesized STn-MIP particles possess selectivity and can be well used for the ratiometric detection of biomarkers such as STn, which are commonly very difficult to target by supramolecular or biomacromolecular indicators or binders in simple assay formats. Motivated by these promising results, we proceeded to test the dual fluorescent STn-MIPs in cell staining applications.

Binding Studies of STn-MIP and NIP Nanoparticles to Cancerous Cell Lines (BxPC-3, CFPAC-1). Previous studies have shown that STn was expressed in tissues of 97% of pancreatic cancers, in contrast to its complete absence in normal pancreas tissue as determined by the monoclonal STn-antibody TKH2.[56] We thus examined the level of STn expression in two pancreatic ductal adenocarcinoma cell lines, BxPC-3 and CFPAC-1, using the STn-antibody TKH2. Immunostaining showed that CFPAC-1 cells were positive to the STn-antibody TKH2, while BxPC-3 cells had no staining signal (Figure 7A). Since the cells in immune staining were permeabilized by Triton X-100, STn located on the cell surface and in the cell cytosol can both be detected. Hence, flow cytometry analysis was performed to examine the staining of STn-antibody TKH2 on the cell surface of the two investigated cell lines. The result revealed that 46.46% CFPAC-1 cells were positive, while BxPC-3 cells remained negative to STn-antibody TKH2 (Figures 7B,C and S7).

After having examined STn-antibody TKH2 staining of BxPC-3 and CFPAC-1 cells, the performance of STn-MIPs was tested on these two cell lines. Here, NIPs, synthesized without STn-Thr-Na as the template, served as a negative control for STn-MIPs. CFPAC-1 cells were first stained with STn-MIPs and NIPs and imaged by fluorescence microscopy, proving that both the emission of dye **1** (green channel) and R-CNDs (red channel) were visible and that STn-MIPs appeared to bind more to the cell surface than to NIPs (Figure 8A). The analysis

https://doi.org/10.1021/acsanm.2c03252
ACS Appl. Nano Mater. XXXX, XXX, XXX−XXX

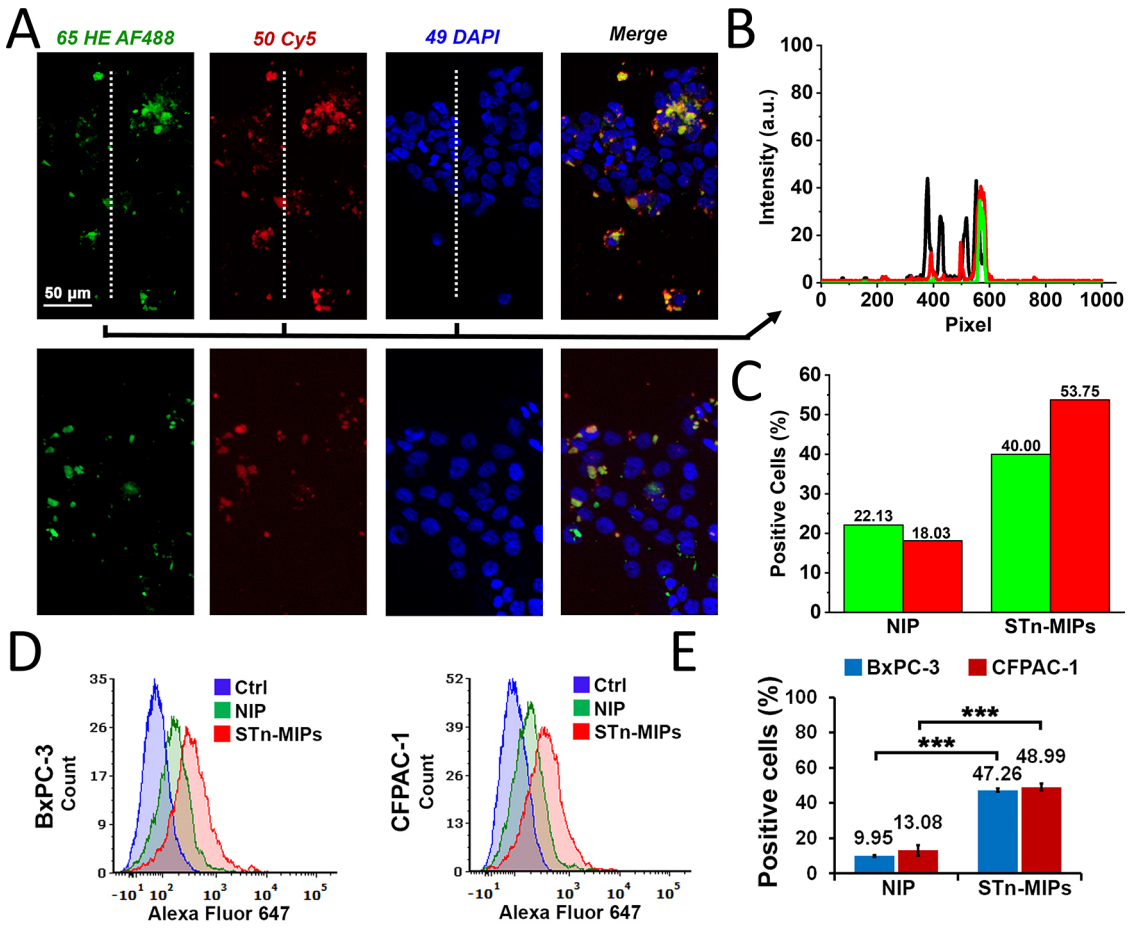

Figure 8. (A) CFPAC-1 cells were stained with STn-MIPs (top) and NIPs (bottom) and analyzed by a fluorescence microscope in the green channel (65 HE AF488) and the red channel (50 Cy5), scale bar: 50 μm; (B) representative histogram of ImageJ analysis of images: black, red, and green curves represent intensity traces along the three dotted lines of (A); (C) percentage of positive cells analyzed from green (in green) and red (in red) channels via the ImageJ-based method; (D) analysis of the staining of BxPC-3 and CFPAC-1 cell lines with STn-MIPs and NIPs by flow cytometry, and (E) percentage of positive cells from the flow cytometry analysis.

of staining images (Figure S8) was performed with an ImageJ-based method.[57] Briefly, the intensity by gray value was plotted using the "*Plot Profile*" function for 27 lines of exactly the same area for all six images, e.g., both STn-MIP and NIP staining images from three channels. Afterward, the total number of cells and bound nanoparticles were summed up and used for the calculation of the percentage of positive cells (experimental details can be found in the Supporting Information).

Figures S9 and S10 show all of the results from ImageJ analysis where black peaks represent the cells and green and red peaks the STn-MIPs or NIPs, emitting from the MIP shell (green) and from the nanoparticle core (red), respectively. Only if red or green peaks were close to black peaks, binding of STn-MIPs to the cells happened and therefore cells were counted as positively stained cells. For instance, from the plot exemplarily shown in Figure 8B, three cells were stained positively from the red channel, while only one positively stained cell was found from the green channel. This could be due to multiple surface-appended glycans binding in the MIP layer, entailing a rather pronounced overall quenching, or to local environmental effects, which might modulate the green fluorescence of **1** in the open MIP network, while the red fluorescence remained largely unchanged. The positively stained cells by STn-MIP/NIPs from red and green channels were 53.75/18.03% and 40.00/22.13%, respectively (Figure 8C).

Moreover, despite the fact that the STn-MIPs show a good dispersibility in aqueous media, agglomerates are frequently encountered in cell staining studies especially when working with fixed cells on microscope slides, most likely resulting from incubation when sonication is not possible anymore. Measurements in suspension might thus still be a better alternative for MIP-based cell analysis, which is why flow cytometric assays were conducted subsequently. Accordingly, CFPAC-1 and BxPC-3 cells were stained with STn-MIPs and NIPs, and the amount of STn-MIP- and NIP-labeled cells was quantified by flow cytometry analysis. It is important to note that quantification in flow cytometry is related to labeled cells, including their biological variability, and not to immediate concentrations of individual STn-terminating glycans as in the STn detection presented in the spectroscopic studies above.

According to flow cytometry analysis, we observed that STn-MIPs stained 48.99% of CFPAC-1 cells, in contrast to NIPs that only stained 13.08% of CFPAC-1 cells (Figures 8D,E and S11). The percentage of STn-MIP-positive cells was almost 4-fold higher than that of NIPs, suggesting that STn-MIPs showed high selectivity in binding to CFPAC-1 cells. Moreover, the immunofluorescence imaging data obtained via the red channel (53.75% vs 18.03% in Figure 8C) agree

https://doi.org/10.1021/acsanm.2c03252
ACS Appl. Nano Mater. XXXX, XXX, XXX−XXX

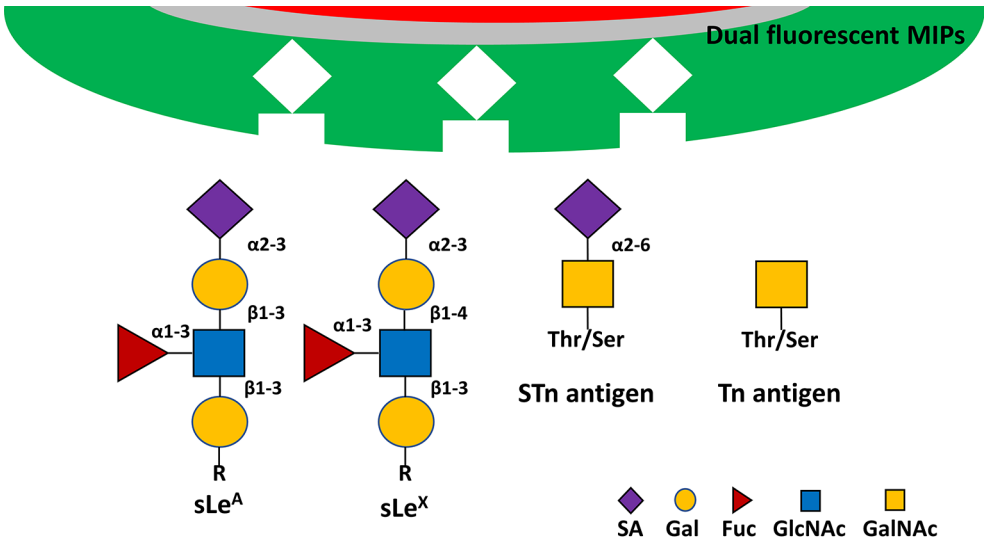

Figure 9. Cancer glycan epitopes with relevance to this work.

well with the FACS results (48.99% vs 13.08% in Figure 8E), indicating an improved accuracy was obtained using dual fluorescent MIPs in comparison with plain core and single-signal MIP shell cases (for instance, only green fluorescence from MIP shell) where no referenced signal is available. Particularly, if no flow cytometer is available, more accurate results from immunofluorescence imaging can be obtained using the presented dual-color MIP labeling. Interestingly, around 47% of BxPC-3 cells showed positive staining by STn-MIPs compared to only 10% in the case of NIPs ($p < 0.001$, Figure 8D,E). This means that there is almost no difference between STn-MIP-stained CFPAC-1 (48.99%) and BxPC-3 (47.26%) cells, which leads to the conclusion that STn-MIPs do not discriminate STn-positive cells from STn-negative ones.

As STn consists of SA bound to a GalNAc (Figures 1A and 9), the STn-MIPs will probably target not only STn but also other cancer glycan epitopes carrying SA and a second saccharide unit in a linear fashion such as the sialyl Lewis^A (sLe^A or CA19-9) antigen on the cell surface (Figure 9). The latter, for instance, has been reported to be expressed on BxPC-3 cells to a significant extent.[58] Hence, the similar binding of STn-MIPs to BxPC-3 and CFPAC-1 might be assigned to the inability of the STn-MIPs to discriminate between STn and sLe^A. As BxPC-3 cells were found to show only low expression levels of Tn, the binding of the STn-MIPs to this imprinted subunit seems to be less likely.[59] The expression of Tn on these two cell lines was thus also examined. Both cell lines were stained using the monoclonal Tn antibody 5F4. The immunofluorescence results revealed that CFPAC-1 and BxPC-3 cell lines stained positive to Tn antibody 5F4, yet flow cytometry analysis showed that the expression level on the surface of both cell lines was indeed low (ca. 1%) (Figure S12).

To verify whether the attachment of the terminal SA group to the glycan chain via linkage to other sugar residues such as Gal by α-2,3 or α-2,6 configuration is responsible for the staining patterns observed here, the expression levels of SA on BxPC-3 and CFPAC-1 cells were further investigated with the biotinylated lectins SNA, MAL I, and MAL II. Previous studies suggested that α-2,6 SA can be detected by SNA,[60−62] while α-2,3 SA can be recognized by both MAL I[63,64] and MAL II.[60−62] The flow cytometry analysis revealed that more than 90% of BxPC-3 and CFPAC-1 cells are positive to SNA, MAL I, and MAL II (Figure S13). These data showed that STn-MIPs presumably bind mainly to STn on CFPAC-1 cells and mainly to sLe^A on BxPC-3 cells.

Overall, cell binding studies revealed that STn-MIPs had a significantly higher ability to bind to STn-positive CFPAC-1 cells as compared to the NIPs. The NIPs labeling 10% of the cells could be attributed to the nonspecific binding that is well known for this kind of molecularly imprinted nanoparticles. However, here, STn-MIPs failed to discriminate the STn-positive cell line CFPAC-1 from the STn-negative cell line BxPC-3, most likely because the latter expresses significant amounts of sLe^A. As the MIPs can only bind to the cell surface via sites that are open, allowing insertion of a short linear oligomeric molecular fragment protruding from the cell surface, the polymer's flexibility—in other words, the degree of cross-linking—close to the outer MIP surface determines the discrimination ability. A typical RAFT polymerization is known to result primarily in a brush-type structure toward the outer surface, possibly making the growth of a homogeneously dense and rigidly cross-linked polymer layer with highly discriminative yet open cavities very challenging. In future, other polymerization strategies in combination with highly specific templates such as STn might pave the way to still better discriminating MIP-based cell staining probes.

■ CONCLUSIONS

In our present work, spectroscopic studies of the complex of fluorescent monomer **1** and NaOAc, as a model analyte, were carried out. These investigations revealed that despite **1** is deprotonated in highly polar and hydrogen bond-accepting solvents such as DMSO and DMF, traceable from optical spectroscopy, hydrogen bonding between **1**$^-$ and the model analyte is still effective as the ^{1}H NMR titration data suggests. Fluorescence studies further indicated that especially DMF should be a suitable porogen as **1**$^-$ is reprotonated already upon optical excitation. Utilizing these interactions, a fluorescent polymer layer, in which STn-Thr-Na was imprinted with **1** and other comonomers and a cross-linker, was synthesized at the surface of R-CSNs, serving as a dual fluorescent MIP probe for the detection of STn-Thr-Na. Fluorescence measurements showed that for STn-MIPs and

https://doi.org/10.1021/acsanm.2c03252
ACS Appl. Nano Mater. XXXX, XXX, XXX−XXX

NIPs both, red and green emission bands were visible under 410 nm excitation, exhibiting the desired behavior of an internally referenced system. However, the red carbon nanodot emission remained virtually unchanged, the green emission stemming from fluorescent monomer **1** showed a selective response upon the addition of STn-Thr-Na, qualifying the system for future use in bioanalytical assays. Immunofluorescence investigation of the binding behaviors of STn-MIPs and NIPs to the pancreatic cancer cellline, CFPAC-1 (STn-positive), further revealed that both emissions, red and green, could be detected individually and correlatedly in two separate channels. An ImageJ-based analysis of immunofluorescence images showed an improved imaging accuracy since the analysis result from the red channel (reference signal) is closer than that from the green channel (response signal) to flow cytometric cell analysis results, e.g., the binding of STn-MIPs was significantly higher than that of NIPs within the same cell line, rendering such measurements more reliable and, ultimately, paving the way to internally referenced stains. STn-MIPs were not able to discriminate STn-positive (CFPAC-1) from STn-negative (BxPC-3) cell lines, which can be assigned to the presence of SA moieties being expressed on both cell lines with the next units in the short *O*-glycan chain differing only to a minor degree (Figure 9). A closer analysis of previous works published on glycan MIP staining of cancer cells points into the same direction, i.e., there is usually a good discrimination between MIPs and NIPs, but the staining patterns as a function of the glycan expression on the cell lines used are seldom discussed or investigated, the predominant epitopes being sLe^X and sLe^A (Table S3 and Figure 9).[14−18,41,65−70] If MIPs should outperform lectins and antibodies in the future, they would need to be optimized, for instance, (i) by creating a more homogeneous polymer network using a feeding approach, (ii) produced against better matching templates, and (iii) tuning the surface of MIP layers by further functionalization, for instance, PEGylation, aiming at a reduction of nonspecific binding. Additionally, studies looking in more detail into the glycan expression on cells are required, possibly including engineered cell lines that for instance do not express SA. Such attempts are currently under way in our laboratories.

In conclusion, it was shown here for the first time that a tumor-associated glycan (STn) imprinted dual fluorescent nanoprobe enables dual-color cancer cell imaging. Both the convenient, feasible, and generic synthetic strategy of the nanoprobe platform and the plausible interaction mechanism between the fluorescent reporter and inorganic ion-paired carboxylate allow for the fabrication of dual fluorescent probes and, ultimately, sensors for the determination of a larger number of disease-related analytes, the modular architecture also allowing for the implementation of multiplexing features by pairing coded cores with analyte-selective fluorescent shells or layers.[71]

■ ASSOCIATED CONTENT

Supporting Information

The Supporting Information is available free of charge at https://pubs.acs.org/doi/10.1021/acsanm.2c03252.

Experimental procedures; determination of equilibrium constants; ImageJ-based analysis of immunofluorescence images; statistical analysis; correlation of the longest wavelength absorption maxima with various different solvent polarities; absorption, excitation, and emission spectra; linear regression of equilibrium constants with calculated parameters of different sodium salts; TEM images; TGA plots; ζ-potentials; dot plots and histograms from cytometry; fluorescence microscopy images; and measurement uncertainties (PDF)

■ AUTHOR INFORMATION

Corresponding Authors

Kornelia Gawlitza − *Chemical and Optical Sensing Division (1.9), Bundesanstalt für Materialforschung und -prüfung (BAM), D-12489 Berlin, Germany;* orcid.org/0000-0002-2043-4522; Email: kornelia.gawlitza@bam.de

Jenny L. Persson − *Department of Molecular Biology, Umeå University, S-901 87 Umeå, Sweden; Division of Experimental Cancer Research, Department of Translational Medicine, Clinical Research Centre, Lund University, S-214 28 Malmö, Sweden*; Email: jenny.persson@umu.se

Authors

Shan Jiang − *Chemical and Optical Sensing Division (1.9), Bundesanstalt für Materialforschung und -prüfung (BAM), D-12489 Berlin, Germany*

Tianyan Wang − *Department of Molecular Biology, Umeå University, S-901 87 Umeå, Sweden*

Sandra Behren − *Department of Chemistry, Umeå University, S-901 87 Umeå, Sweden*

Ulrika Westerlind − *Department of Chemistry, Umeå University, S-901 87 Umeå, Sweden*

Knut Rurack − *Chemical and Optical Sensing Division (1.9), Bundesanstalt für Materialforschung und -prüfung (BAM), D-12489 Berlin, Germany;* orcid.org/0000-0002-5589-5548

Complete contact information is available at: https://pubs.acs.org/10.1021/acsanm.2c03252

Author Contributions

[⊥]S.J. and T.W. contributed equally. S.J., T.W., K.G., J.L.P., and K.R. conceived the experiments. S.J. and T.W. performed the experiments. S.B. and U.W. planned and synthesized the STn-Thr-Na. S.J., K.G., and K.R. together with T.W. and J.L.P. wrote the manuscript. All authors discussed the results and commented on the manuscript. All authors have given approval to the final version of the manuscript.

Notes

The authors declare no competing financial interest.

■ ACKNOWLEDGMENTS

This work has received funding from the European Union's Horizon 2020 Research and Innovation Programme under the Marie Skłodowska−Curie Grant Agreement No. 721297. The authors thank M. Grüneberg (BAM) for TGA measurement, J. Falkenhagen (BAM) for ATR-FTIR measurements, A. Zehl (Humboldt University Berlin, HUB) for elemental analysis, and M. Kimani (BAM) for the advice on the determination of the dissociation constant.

■ REFERENCES

(1) Ohtsubo, K.; Marth, J. D. Glycosylation in cellular mechanisms of health and disease. *Cell* **2006**, *126*, 855−867.

(2) Hounsell, E. F.; Davies, M. J.; Renouf, D. V. O-linked protein glycosylation structure and function. *Glycoconjugate J.* **1996**, *13*, 19−26.
(3) Kailemia, M. J.; Park, D.; Lebrilla, C. B. Glycans and glycoproteins as specific biomarkers for cancer. *Anal. Bioanal. Chem.* **2017**, *409*, 395−410.
(4) Pinho, S. S.; Reis, C. A. Glycosylation in cancer: mechanisms and clinical implications. *Nat. Rev. Cancer* **2015**, *15*, 540−555.
(5) Poiroux, G.; Barre, A.; van Damme, E. J. M.; Benoist, H.; Rouge, P. Plant lectins targeting O-glycans at the cell surface as tools for cancer diagnosis, prognosis and therapy. *Int. J. Mol. Sci.* **2017**, *18*, 1232.
(6) Ruhaak, L. R.; Miyamoto, S.; Lebrilla, C. B. Developments in the Identification of Glycan Biomarkers for the Detection of Cancer. *Mol. Cell. Proteomics* **2013**, *12*, 846−855.
(7) Striegler, S. Selective carbohydrate recognition by synthetic receptors in aqueous solution. *Curr. Org. Chem.* **2003**, *7*, 81−102.
(8) Dosekova, E.; Filip, J.; Bertok, T.; Both, P.; Kasak, P.; Tkac, J. Nanotechnology in Glycomics: Applications in Diagnostics, Therapy, Imaging, and Separation Processes. *Med. Res. Rev.* **2017**, *37*, 514−626.
(9) Chen, Y.; Huang, A. L.; Zhang, Y. N.; Bie, Z. J. Recent advances of boronate affinity materials in sample preparation. *Anal. Chim. Acta* **2019**, *1076*, 1−17.
(10) Gao, S. H.; Wang, W.; Wang, B. H. Building fluorescent sensors for carbohydrates using template-directed polymerizations. *Bioorg. Chem.* **2001**, *29*, 308−320.
(11) Basabe-Desmonts, L.; Reinhoudt, D. N.; Crego-Calama, M. Design of fluorescent materials for chemical sensing. *Chem. Soc. Rev.* **2007**, *36*, 993−1017.
(12) Gawlitza, K.; Wan, W.; Wagner, S.; Rurack, K.Fluorescent Molecularly Imprinted Polymers. In *Advanced Molecular Imprinting Materials*; Tiwari, A.; Uzun, L., Eds.; Wiley-Scrivener: Beverly, MA, 2017; pp 89−128.
(13) Keçili, R.; Buyuktiryaki, S.; Hussain, C. M. Advancement in bioanalytical science through nanotechnology: Past, present and future. *TrAC, Trends Anal. Chem.* **2019**, *110*, 259−276.
(14) Kunath, S.; Panagiotopoulou, M.; Maximilien, J.; Marchyk, N.; Saenger, J.; Haupt, K. Cell and tissue imaging with molecularly imprinted polymers as plastic antibody mimics. *Adv. Healthcare Mater.* **2015**, *4*, 1322−1326.
(15) Shinde, S.; El-Schich, Z.; Malakpour, A.; Wan, W.; Dizeyi, N.; Mohammadi, R.; Rurack, K.; Wingren, A. G.; Sellergren, B. Sialic Acid-Imprinted Fluorescent Core-Shell Particles for Selective Labeling of Cell Surface Glycans. *J. Am. Chem. Soc.* **2015**, *137*, 13908−13912.
(16) Wang, S. S.; Yin, D. Y.; Wang, W. J.; Shen, X. J.; Zhu, J. J.; Chen, H. Y.; Liu, Z. Targeting and Imaging of Cancer Cells via Monosaccharide-Imprinted Fluorescent Nanoparticles. *Sci. Rep.* **2016**, *6*, No. 22757.
(17) Panagiotopoulou, M.; Kunath, S.; Medina-Rangel, P. X.; Haupt, K.; Bui, B. T. S. Fluorescent molecularly imprinted polymers as plastic antibodies for selective labeling and imaging of hyaluronan and sialic acid on fixed and living cells. *Biosens. Bioelectron.* **2017**, *88*, 85−93.
(18) Demir, B.; Lemberger, M. M.; Panagiotopoulou, M.; Rangel, P. X. M.; Timur, S.; Hirsch, T.; Bui, B. T. S.; Wegener, J.; Haupt, K. Tracking Hyaluronan: Molecularly Imprinted Polymer Coated Carbon Dots for Cancer Cell Targeting and Imaging. *ACS Appl. Mater. Interfaces* **2018**, *10*, 3305−3313.
(19) Haupt, K.; Rangel, P. X. M.; Bui, B. T. S. Molecularly Imprinted Polymers: Antibody Mimics for Bioimaging and Therapy. *Chem. Rev.* **2020**, *120*, 9554−9582.
(20) Zhang, R.; Zhang, T.; Lv, Y.; Qin, P.; Li, H.; Li, J.-P.; Tan, T. Selective binding of heparin oligosaccharides in a magnetic thermoresponsive molecularly imprinted polymer. *Talanta* **2019**, *201*, 441−449.
(21) Li, J.; Ma, X.; Li, M.; Zhang, Y. Does polysaccharide is an idea template selection for glycosyl imprinting? *Biosens. Bioelectron.* **2018**, *99*, 438−442.
(22) Li, F. J.; Ding, J. J. Sialylation is involved in cell fate decision during development, reprogramming and cancer progression. *Protein Cell* **2019**, *10*, 550−565.
(23) He, L.; Lu, D.-Q.; Liang, H.; Xie, S.; Luo, C.; Hu, M.; Xu, L.; Zhang, X.; Tan, W. Fluorescence Resonance Energy Transfer-Based DNA Tetrahedron Nanotweezer for Highly Reliable Detection of Tumor-Related mRNA in Living Cells. *ACS Nano* **2017**, *11*, 4060−4066.
(24) Wang, X.; Qin, L.; Lin, M.; Xing, H.; Wei, H. Fluorescent Graphitic Carbon Nitride-Based Nanozymes with Peroxidase-Like Activities for Ratiometric Biosensing. *Anal. Chem.* **2019**, *91*, 10648−10656.
(25) Harmsen, S.; Medine, E. I.; Moroz, M.; Nurili, F.; Lobo, J.; Dong, Y.; Turkekul, M.; Pillarsetty, N. V. K.; Ting, R.; Ponomarev, V.; et al. A dual-modal PET/near infrared fluorescent nanotag for long-term immune cell tracking. *Biomaterials* **2021**, *269*, No. 120630.
(26) Yang, Y.; Zhu, J.; Weng, G.-J.; Li, J.-J.; Zhao, J.-W. Gold nanoring core-shell satellites with abundant built-in hotspots and great analyte penetration: An immunoassay platform for the SERS/fluorescence-based detection of carcinoembryonic antigen. *J. Chem. Eng.* **2021**, *409*, No. 128173.
(27) Wan, W.; Biyikal, M.; Wagner, R.; Sellergren, B.; Rurack, K. Fluorescent sensory microparticles that "light-up" consisting of a silica core and a molecularly imprinted polymer (MIP) shell. *Angew. Chem., Int. Ed.* **2013**, *52*, 7023−7027.
(28) Wagner, S.; Bell, J.; Biyikal, M.; Gawlitza, K.; Rurack, K. Integrating fluorescent molecularly imprinted polymer (MIP) sensor particles with a modular microfluidic platform for nanomolar small-molecule detection directly in aqueous samples. *Biosens. Bioelectron.* **2018**, *99*, 244−250.
(29) Pan, L.; Sun, S.; Zhang, L.; Jiang, K.; Lin, H. Near-infrared emissive carbon dots for two-photon fluorescence bioimaging. *Nanoscale* **2016**, *8*, 17350−17356.
(30) Santra, S.; Bagwe, R. P.; Dutta, D.; Stanley, J. T.; Walter, G. A.; Tan, W.; Moudgil, B. M.; Mericle, R. A. Synthesis and characterization of fluorescent, radio-opaque, and paramagnetic silica nanoparticles for multimodal bioimaging applications. *Adv. Mater.* **2005**, *17*, 2165−2169.
(31) Igathinathane, C.; Pordesimo, L. O.; Columbus, E. P.; Batchelor, W. D.; Methuku, S. R. Shape identification and particles size distribution from basic shape parameters using ImageJ. *Comput. Electron. Agric.* **2008**, *63*, 168−182.
(32) Nicholls, I. A. Towards the rational design of molecularly imprinted polymers. *J. Mol. Recognit.* **1998**, *11*, 79−82.
(33) Wan, W.; Wagner, S.; Rurack, K. Fluorescent monomers: "bricks" that make a molecularly imprinted polymer "bright". *Anal. Bioanal. Chem.* **2016**, *408*, 1753−1771.
(34) Liang, L.; Liu, Z. A self-assembled molecular team of boronic acids at the gold surface for specific capture of cis-diol biomolecules at neutral pH. *Chem. Commun.* **2011**, *47*, 2255−2257.
(35) Descalzo, A. B.; Rurack, K.; Weisshoff, H.; Martinez-Manez, R.; Marcos, M. D.; Amoros, P.; Hoffmann, K.; Soto, J. Rational design of a chromo- and fluorogenic hybrid chemosensor material for the detection of long-chain carboxylates. *J. Am. Chem. Soc.* **2005**, *127*, 184−200.
(36) Gunnlaugsson, T.; Glynn, M.; Tocci, G. M.; Kruger, P. E.; Pfeffer, F. M. Anion recognition and sensing in organic and aqueous media using luminescent and colorimetric sensors. *Coord. Chem. Rev.* **2006**, *250*, 3094−3117.
(37) Ding, L.; Yu, H.; Lau, K.; Li, Y.; Muthana, S.; Wang, J.; Chen, X. Efficient chemoenzymatic synthesis of sialyl Tn-antigens and derivatives. *Chem. Commun.* **2011**, *47*, 8691−8693.
(38) Zhang, Y.; Song, D.; Brown, J. C.; Shimizu, K. D. Suppression of background sites in molecularly imprinted polymers via urea-urea monomer aggregation. *Org. Biomol. Chem.* **2011**, *9*, 120−126.
(39) Wagner, S.; Zapata, C.; Wan, W.; Gawlitza, K.; Weber, M.; Rurack, K. Role of counterions in molecularly imprinted polymers for anionic species. *Langmuir* **2018**, *34*, 6963−6975.

https://doi.org/10.1021/acsanm.2c03252
ACS Appl. Nano Mater. XXXX, XXX, XXX−XXX

(40) Tarai, A.; Baruah, J. B. Conformation and visual distinction between urea and thiourea derivatives by an acetate ion and a hexafluorosilicate cocrystal of the urea derivative in the detection of water in dimethylsulfoxide. *ACS Omega* **2017**, *2*, 6991−7001.
(41) Kimani, M.; Beyer, S.; El-Schich, Z.; Gawlitza, K.; Gjörloff-Wingren, A.; Rurack, K. Imprinted Particles for Direct Fluorescence Detection of Sialic Acid in Polar Media and on Cancer Cells with Enhanced Control of Nonspecific Binding. *ACS Appl. Polym. Mater.* **2021**, *3*, 2363−2373.
(42) Wan, W.; Descalzo, A. B.; Shinde, S.; Weisshoff, H.; Orellana, G.; Sellergren, B.; Rurack, K. Ratiometric Fluorescence Detection of Phosphorylated Amino Acids Through Excited-State Proton Transfer by Using Molecularly Imprinted Polymer (MIP) Recognition Nanolayers. *Chem. − Eur. J.* **2017**, *23*, 15974−15983.
(43) Zengin, A.; Karakose, G.; Caykara, T. Poly(2-(dimethylamino)-ethyl methacrylate) brushes fabricated by surface-mediated RAFT polymerization and their response to pH. *Eur. Polym. J.* **2013**, *49*, 3350−3358.
(44) Liu, F.; Urban, M. W. Dual temperature and pH responsiveness of poly(2-(N,N-dimethylamino)ethyl methacrylate-co-n-butyl acrylate) colloidal dispersions and their films. *Macromolecules* **2008**, *41*, 6531−6539.
(45) Kugimiya, A.; Yoneyama, H.; Takeuchi, T. Sialic Acid Imprinted Polymer-Coated Quartz Crystal Microbalance. *Electroanalysis* **2000**, *12*, 1322−1326.
(46) Kugimiya, A.; Matsui, J.; Takeuchi, T.; Yano, K.; Muguruma, H.; Elgersma, A. V.; Karube, I. Recognition of Sialic-Acid Using Molecularly Imprinted Polymer. *Anal. Lett.* **1995**, *28*, 2317−2323.
(47) Piletsky, S. A.; Piletskaya, E. V.; Yano, K.; Kugimiya, A.; Elgersma, A. V.; Levi, R.; Kahlow, U.; Takeuchi, T.; Karube, I.; Panasyuk, T. I.; El'skaya, A. V. A Biomimetic Receptor System for Sialic Acid Based on Molecular Imprinting. *Anal. Lett.* **1996**, *29*, 157−170.
(48) Burns, A.; Ow, H.; Wiesner, U. Fluorescent core-shell silica nanoparticles: towards "Lab on a Particle" architectures for nanobiotechnology. *Chem. Soc. Rev.* **2006**, *35*, 1028−1042.
(49) Gui, R.; Jin, H.; Bu, X.; Fu, Y.; Wang, Z.; Liu, Q. Recent advances in dual-emission ratiometric fluorescence probes for chemo/biosensing and bioimaging of biomarkers. *Coord. Chem. Rev.* **2019**, *383*, 82−103.
(50) Thurn, K. T.; Brown, E. M. B.; Wu, A.; Vogt, S.; Lai, B.; Maser, J.; Paunesku, T.; Woloschak, G. E. Nanoparticles for applications in cellular Imaging. *Nanoscale Res. Lett.* **2007**, *2*, 430−441.
(51) Xiao, D. L.; Su, L. J.; Teng, Y.; Hao, J. F.; Bi, Y. P. Fluorescent nanomaterials combined with molecular imprinting polymer: synthesis, analytical applications, and challenges. *Microchim. Acta* **2020**, *187*, 399.
(52) Ansari, S.; Masoum, S. Recent advances and future trends on molecularly imprinted polymer-based fluorescence sensors with luminescent carbon dots. *Talanta* **2021**, *223*, No. 121411.
(53) Murugan, K.; Jothi, V. K.; Rajaram, A.; Natarajan, A. Novel Metal-Free Fluorescent Sensor Based on Molecularly Imprinted Polymer N-CDs@ MIP for Highly Selective Detection of TNP. *ACS Omega* **2022**, *7*, 1368−1379.
(54) Weissleder, R. A clearer vision for in vivo imaging. *Nat. Biotechnol.* **2001**, *19*, 316−317.
(55) Carbonaro, C. M.; Chiriu, D.; Stagi, L.; Casula, M. F.; Thakkar, S. V.; Malfatti, L.; Suzuki, K.; Ricci, P. C.; Corpino, R. Carbon Dots in Water and Mesoporous Matrix: Chasing the Origin of their Photoluminescence. *J. Phys. Chem. C* **2018**, *122*, 25638−25650.
(56) Itzkowitz, S.; Kjeldsen, T.; Friera, A.; Hakomori, S. I.; Yang, U. S.; Kim, Y. S. Expression of Tn, sialosyl Tn, and T antigens in human pancreas. *Gastroenterology* **1991**, *100*, 1691−1700.
(57) Collins, T. J. ImageJ for microscopy. *BioTechniques* **2007**, *43*, S25−S30.
(58) Liu, C.; Deng, S. M.; Jin, K. Z.; Gong, Y. T.; Cheng, H.; Fan, Z. Y.; Qian, Y. Z.; Huang, Q. Y.; Ni, Q. X.; Luo, G. P.; Yu, X. J. Lewis antigen-negative pancreatic cancer: An aggressive subgroup. *Int. J. Oncol.* **2020**, *56*, 900−908.
(59) Hofmann, B. T.; Schluter, L.; Lange, P.; Mercanoglu, B.; Ewald, F.; Folster, A.; Picksak, A. S.; Harder, S.; El Gammal, A. T.; Grupp, K.; Gungor, C.; Drenckhan, A.; Schluter, H.; Wagener, C.; Izbicki, J. R.; Jucker, M.; Bockhorn, M.; Wolters-Eisfeld, G. COSMC knockdown mediated aberrant O-glycosylation promotes oncogenic properties in pancreatic cancer. *Mol. Cancer* **2015**, *14*, 109.
(60) Verkoelen, C. F.; van der Boom, B. G.; Kok, D. J.; Romijn, J. C. Sialic acid and crystal binding. *Kidney Int.* **2000**, *57*, 1072−1082.
(61) Han, J.; Perez, J. T.; Chen, C.; Li, Y.; Benitez, A.; Kandasamy, M.; Lee, Y.; Andrade, J.; Tenoever, B.; Manicassamy, B. Genome-wide CRISPR/Cas9 Screen Identifies Host Factors Essential for Influenza Virus Replication. *Cell Rep.* **2018**, *23*, 596−607.
(62) Lomax-Browne, H. J.; Robertson, C.; Antonopoulos, A.; Leathem, A. J. C.; Haslam, S. M.; Dell, A.; Dwek, M. V. Serum IgA1 shows increased levels of alpha 2,6-linked sialic acid in breast cancer. *Interface Focus* **2019**, *9*, No. 20180079.
(63) Nokhbeh, M. R.; Hazra, S.; Alexander, D. A.; Khan, A.; McAllister, M.; Suuronen, E. J.; Griffith, M.; Dimock, K. Enterovirus 70 binds to different glycoconjugates containing alpha 2,3-linked sialic acid on different cell lines. *J. Virol.* **2005**, *79*, 7087−7094.
(64) Shen, L.; Luo, Z.; Wu, J.; Qiu, L.; Lu, M.; Ke, Q.; Dong, X. Enhanced expression of alpha 2,3-linked sialic acids promotes gastric cancer cell metastasis and correlates with poor prognosis. *Int. J. Oncol.* **2017**, *50*, 1201−1212.
(65) Liu, R. H.; Cui, Q. L.; Wang, C.; Wang, X. Y.; Yang, Y.; Li, L. D. Preparation of Sialic Acid-Imprinted Fluorescent Conjugated Nanoparticles and Their Application for Targeted Cancer Cell Imaging. *ACS Appl. Mater. Interfaces* **2017**, *9*, 3006−3015.
(66) El-Schich, Z.; Abdullah, M.; Shinde, S.; Dizeyi, N.; Rosen, A.; Sellergren, B.; Wingren, A. G. Different expression levels of glycans on leukemic cells-a novel screening method with molecularly imprinted polymers (MIP) targeting sialic acid. *Tumor Biol.* **2016**, *37*, 13763−13768.
(67) Patel, M.; Feith, M.; Janicke, B.; Alm, K.; El-Schich, Z. Evaluation of the Impact of Imprinted Polymer Particles on Morphology and Motility of Breast Cancer Cells by Using Digital Holographic Cytometry. *Appl. Sci.* **2020**, *10*, 750.
(68) Wang, S. S.; Wen, Y. R.; Wang, Y. J.; Ma, Y. Y.; Liu, Z. Pattern Recognition of Cells via Multiplexed Imaging with Monosaccharide-Imprinted Quantum Dots. *Anal. Chem.* **2017**, *89*, 5646−5652.
(69) Gu, Z. K.; Dong, Y. R.; Xu, S. X.; Wang, L. S.; Liu, Z. Molecularly Imprinted Polymer-Based Smart Prodrug Delivery System for Specific Targeting, Prolonged Retention, and Tumor Microenvironment-Triggered Release. *Angew. Chem., Int. Ed.* **2021**, *60*, 2663−2667.
(70) Panagiotopoulou, M.; Salinas, Y.; Beyazit, S.; Kunath, S.; Duma, L.; Prost, E.; Mayes, A. G.; Resmini, M.; Bui, B. T. S.; Haupt, K. Molecularly Imprinted Polymer Coated Quantum Dots for Multiplexed Cell Targeting and Imaging. *Angew. Chem., Int. Ed.* **2016**, *55*, 8244−8248.
(71) Carl, P.; Sarma, D.; Gregório, B. J. R.; Hoffmann, K.; Lehmann, A.; Rurack, K.; Schneider, R. J. Wash-Free Multiplexed Mix-and-Read Suspension Array Fluorescence Immunoassay for Anthropogenic Markers in Wastewater. *Anal. Chem.* **2019**, *91*, 12988−12996.

https://doi.org/10.1021/acsanm.2c03252
ACS Appl. Nano Mater. XXXX, XXX, XXX−XXX